ADVANCED FUNCTIONAL MATERIALS
www.afm-journal.de

Palladium-Induced Localized High-Spin Environment Enhances Redox Kinetics for High-Performance Aqueous Energy Storage

Xin Liu, Yan Yan, Qiaoyi Zhang, Hongtan Cai, Meiyan Wang, Xiliang Gong, Jingchen Zhang, Zeshuo Meng, Haoteng Sun,* Zhengyan Du,* and Xiufeng Hao**

Regulating the surface electronic structure is crucial for the directional design of efficient energy storage materials. However, the mechanisms by which alterations in the spin microenvironment enhance intrinsic energy storage activity remain elusive. In this study, a localized high-spin environment is successfully constructed by modifying the surface of NH_2-UiO-66 derivatives with high-spin configuration palladium (Pd) nanoparticles. By integrating density functional theory calculations, in situ spectroscopy, and multiscale kinetic analysis, it is revealed that the introduction of high-spin state Pd creates a Lewis acidic environment on the electrode surface, which significantly enhances the adsorption capacity and reactivity of electron-rich intermediates. Moreover, the spin polarization effect increases the delocalization of d electrons and introduces new electronic states near the Fermi level, thereby markedly accelerating the kinetics of electrochemical reactions. Benefiting from this mechanism, electrodes with a localized high-spin environment exhibit exceptional energy storage performance, with a high specific capacitance of 773.3 F g^{-1} at 1 A g^{-1}. This study offers novel theoretical insights and technical pathways for the design and fabrication of highly active energy storage electrodes.

1. Introduction

With the rapidly growing demand for smart communication and wearable devices, the development of efficient energy storage technologies has become a critical challenge in the energy sector.[1] Aqueous supercapacitors have attracted considerable attention due to their high power density, rapid charge–discharge capabilities, and ultralong cycle life, demonstrating broad application prospects.[2] Nevertheless, their low energy density remains a major bottleneck for large-scale implementation.[3] Thus, designing electrode materials with high specific capacitance, superior rate performance, and long-term cycling stability is essential for advancing high-performance aqueous energy storage systems.[4] Platinum group metals (PGMs) are considered key materials for next-generation advanced energy storage due to their exceptional conductivity

X. Liu, Y. Yan, Q. Zhang, H. Cai, X. Hao
College of Chemistry
State Key Laboratory of Inorganic Synthesis and Preparative Chemistry
Jilin University
Changchun 130012, P. R. China
E-mail: haoxf@jlu.edu.cn

M. Wang
Department of Physics
Rutgers University
Newark, NJ 07102, USA

X. Gong
Department of Chemistry and Biochemistry
University of Maryland
College Park, MD 20742, USA

J. Zhang
Institute for Physical Science and Technology
University of Maryland
College Park, MD 20742, USA

The ORCID identification number(s) for the author(s) of this article can be found under https://doi.org/10.1002/adfm.202503345

DOI: 10.1002/adfm.202503345

Z. Meng
i-lab
Nano-X Vacuum Interconnected Workstation
Suzhou Institute of Nano-Tech and Nano-Bionics
Chinese Academy of Sciences
Suzhou 215123, P. R. China
E-mail: zsmeng2024@sinano.ac.cn

Z. Meng
School of Nano Technology and Nano Bionics
University of Science and Technology of China
Hefei 230026, P. R. China

H. Sun
Department of Chemistry
Brown University
Providence, RI 02912, USA
E-mail: haoteng_sun@brown.edu

Z. Du
Chinese Academy of Sciences Key Laboratory of Urban Pollutant Conversion
Department of Environmental Science and Engineering
University of Science and Technology of China
Hefei 230026, P. R. China
E-mail: zhengyandu@mail.ustc.edu.cn

and electrochemical stability.[5] Among them, palladium (Pd) stands out as a highly promising candidate owing to its structural flexibility and outstanding physicochemical properties.[6] However, Pd's electronic configuration follows the anti-Aufbau principle and lacks open electron shells, typically resulting in relatively weak chemical reactivity. This inherent limitation restricts its potential for high-energy storage applications.

In recent years, the strategy of tuning the electronic spin states of core elements to tailor high-energy storage active electrode materials has garnered widespread attention.[7] During the energy storage process, the slow spin state transitions of intermediates significantly limit the reaction kinetics. By designing electrode materials with specific spin electronic structures, it is possible to effectively regulate the attack and charge transfer intensity of intermediates, thereby mitigating the impact of spin state transitions on energy storage activity and enhancing reaction efficiency.[8] Fortunately, the 4d orbital electrons of Pd are located at a higher energy level, resulting in a weaker shielding effect. Additionally, the low ionization energy of Pd enables higher electron mobility, allowing it to lose some of its fully filled electrons and form more singly occupied high-spin configurations, thereby creating open electron shells. This characteristic provides a theoretical basis for enhancing its adsorption capacity for intermediates, improving conductivity, and increasing energy storage activity. However, despite these advantages, the underlying mechanism by which high-spin-state Pd enhances surface redox reactions during energy storage remains poorly understood, primarily due to the lack of systematic and in-depth investigations.

Herein, we report a feasible surface modulation strategy that successfully constructs a localized high-spin environment by modifying high-spin configuration Pd nanoparticles on NH_2-UiO-66 derivatives (Pd@ZrO_2-CN-1000). Thanks to this design, the Pd@ZrO_2-CN-1000 electrode material exhibits outstanding energy storage performance, achieving a high specific capacitance of 773.3 F g^{-1} at a current density of 1 A g^{-1}, along with good stability. By combining density functional theory calculations, in situ spectroscopy characterization, and multiscale kinetic simulations, we systematically investigated the regulatory effects of the high-spin environment on the kinetics of surface redox reactions. The study shows that the introduction of high-spin state Pd creates a Lewis acidic environment on the electrode surface, significantly enhancing the adsorption and reactivity of electron-rich intermediates. Additionally, the spin polarization effect increases the delocalization of d electrons and introduces new electronic states near the Fermi level, thereby accelerating the electron transfer process and improving the kinetics of electrochemical reactions. This work clarifies the intrinsic mechanism by which a localized high-spin environment enhances energy storage activity, providing new insights for the design and application of high-performance energy storage electrodes.

2. Results and Discussion

The structural analysis of the samples was systematically conducted using X-ray diffraction (XRD) patterns and Raman spectroscopy. The XRD pattern (**Figure 1a**) shows that all samples exhibit characteristic peaks corresponding to two polymorphs of ZrO_2. Specifically, the diffraction peaks at 30.27°, 35.25°, 50.38°, and 50.71° correspond to the (011), (110), (112), and (020) crystal planes of tetragonal zirconia (t-ZrO_2) (PDF#50-1089), while the peaks at 28.17°, 31.47°, and 34.16° match the (−111), (111), and (200) crystal planes of monoclinic zirconia (m-ZrO_2) (PDF#37-1484). Notably, no signals for Pd were observed in the three Pd-loaded samples, which may be attributed to the small particle size and low content of Pd nanoclusters. Furthermore, after the incorporation of Pd, the intensity of the (110) crystal plane diffraction peak of t-ZrO_2 significantly decreased, indicating that the introduction of Pd has a direct impact on the structure of t-ZrO_2. Compared to the standard XRD peak position of traditional Pd, the (111) peak of Pd in this study shifts negatively. This lattice expansion arises from changes in the eg orbital electron occupancy caused by the Jahn–Teller effect, while the lattice symmetry of traditional Pd is constrained by the low-spin state. Further analysis of the Raman spectrum (Figure S1, Supporting Information) reveals that t-ZrO_2 exhibits six symmetric vibrational modes. Specifically, three peaks of the E_g mode appear at 631, 470, and 260 cm^{-1}, while two peaks of the B_{1g} mode are located at 326 and 140 cm^{-1}, and the peak of the A_{1g} mode appears at 606 cm^{-1}. In the samples after Pd loading (Figure 1b), the full width at half maximum of the characteristic peak ≈630 cm^{-1} increases, which is attributed to the Pd–O vibrational mode. Additionally, the peaks of the E_g and B_{1g} modes show slight shifts, indicating that the addition of Pd enhances the interaction between Pd and O.

To further investigate the loading position of Pd, H_2-TPR tests were conducted. The results (Figure 1c) show that the Pd@ZrO_2-CN-1000 sample exhibits a reverse peak at ≈100 °C, which is associated with the decomposition of palladium hydride (PdH_x), indicating that Pd preferentially reacts with H_2 at low temperatures to form palladium hydride.[9] The positive peak at ≈140 °C corresponds to the reduction of PdO on the catalyst surface,[10] while the peak ≈300 °C indicates the reduction process of Pd–O–Zr.[11] Combined with the EPR test results (Figure S2, Supporting Information), it is confirmed that Pd nanoparticles are successfully loaded onto the surface of ZrO_2 and are anchored in the oxygen vacancies.

The microstructure of the samples was characterized using scanning electron microscopy (SEM) (Figure S3, Supporting Information), revealing a distinct pore structure. BET test results (Figure S4 and Table S1, Supporting Information) further confirm that the samples possess a large specific surface area and abundant mesoporous structures, providing numerous active sites and efficient ionic transport pathways for energy storage reactions. To further analyze the surface characteristics of the materials, transmission electron microscopy (TEM) was employed for imaging studies. TEM results (Figure 1d; Figures S5, S6, Supporting Information) indicate that the Pd@ZrO_2-CN-1000 sample contains a large number of smaller-sized Pd nanoparticles. High-resolution transmission electron microscopy (HRTEM) reveals lattice spacings of 0.32 and 0.30 nm in the sample, corresponding to the (−111) crystal plane of m-ZrO_2 and the (011) crystal plane of t-ZrO_2, respectively (Figure 1e). Additionally, high-angle annular dark field scanning transmission electron microscopy (HAADF-STEM) images and their corresponding X-ray energy dispersive spectroscopy (EDX) elemental mapping (Figure 1f,g) show that the elements C, N, O, Zr, and Pd are uniformly distributed throughout the sample, consistent with the SEM-EDX test results (Figure S3, Supporting Information),

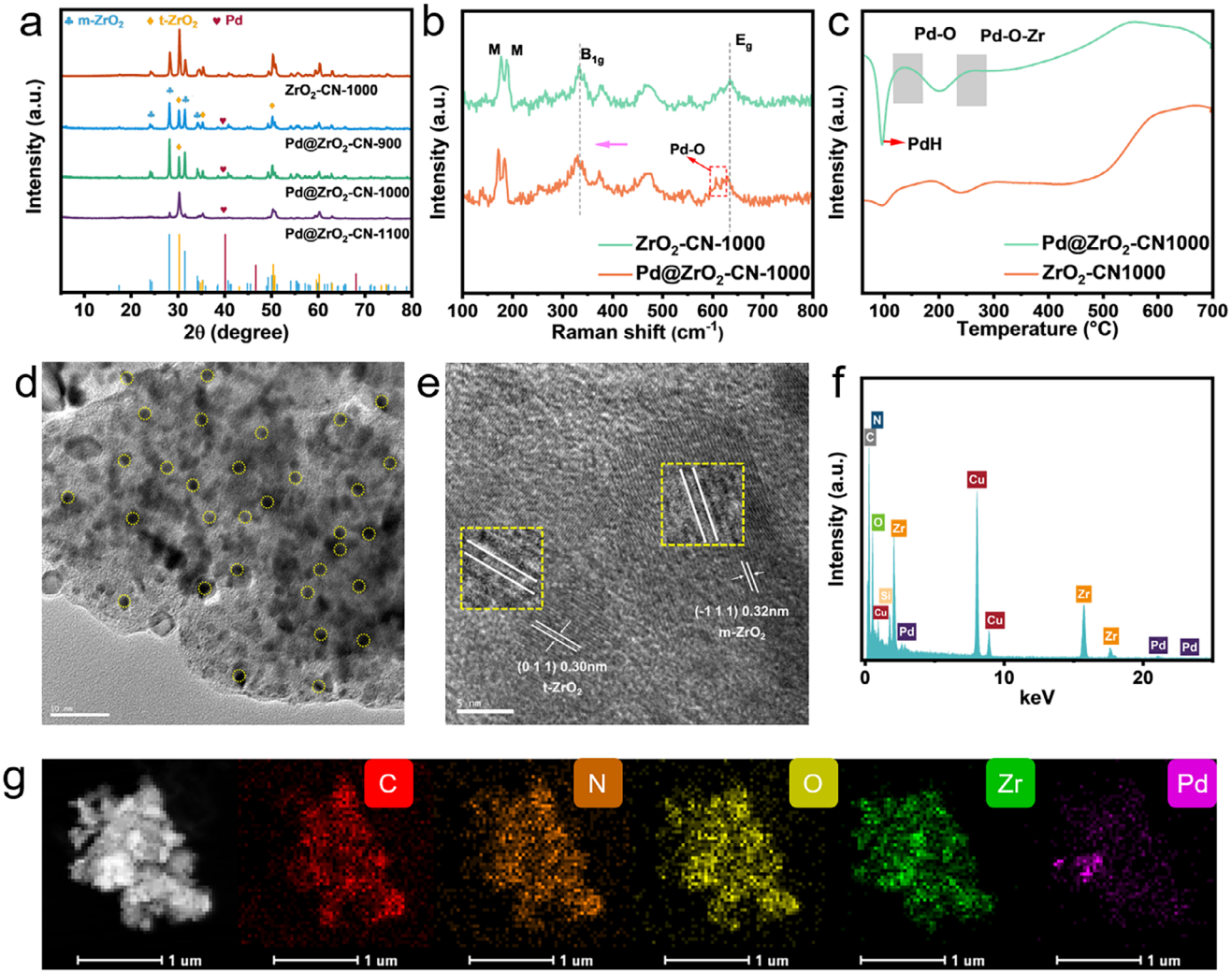

Figure 1. Structural and morphological characterizations of catalysts. a) XRD patterns of ZrO_2-CN-1000 and Pd@ZrO_2-CN-X (X = 900, 1000, and 1100). b) Raman spectra, and c) H_2-TPR curves of ZrO_2-CN-1000 and Pd@ZrO_2-CN-1000. d) TEM image and e) HRTEM image of Pd@ZrO_2-CN-1000. f) EDX patterns and g) HAADF-STEM and corresponding elemental mapping images of Pd@ZrO_2-CN-1000.

further confirming the uniformity and structural features of the sample.

The chemical valence state changes and electron transfer in the Pd-loaded samples were investigated in depth using X-ray photoelectron spectroscopy (XPS) (**Figure** 2a). The wide scan spectrum shows the presence of C, N, O, Zr, and Pd elements in the sample, with the composition distribution meeting expectations (Figure S7, Supporting Information). The XPS carbon spectrum further delineates three main chemical environments for the carbon element, corresponding to C—C, C—O—Zr, and C—O bonds (Figure S8a, Supporting Information). Notably, in the Pd-loaded samples, the peak intensity of the C—O bond significantly decreases (Figure 2b), which is attributed to some Pd being loaded onto the oxygen vacancies, leading to a reduction in the electron density of the C—O bond and thereby weakening its signal intensity. For the O 1s XPS spectrum, after deconvolution (Figure S8b, Supporting Information), characteristic peaks at 530.8, 532.05, 532.75, and 534.00 eV were identified, corresponding to lattice oxygen, oxygen vacancies, adsorbed oxygen, and C—O bonds, respectively. As the annealing temperature increases, the proportion of oxygen vacancies (O_v) gradually decreases, and a new C—OH peak appears at 1100 °C. Simultaneously, the Zr 3d spectrum (Figure S8c, Supporting Information) shows three characteristic peaks after deconvolution analysis: Zr $3d_{5/2}$, Zr $3d_{3/2}$, and Zr—O—C. Analysis indicates that after Pd loading, the positions of the O 1s and Zr 3d peaks in the Pd@ZrO_2-CN-1000 sample redshifted (Figure 2c,d), suggesting that electron transfer occurring during the Pd loading process, with Pd atoms losing electrons and transferring them to Zr and O, resulting in the formation of high-valent species of Pd.[12] This electron redistribution enhances the Lewis acidity of the Pd sites. The Zr 3p and Pd 3d spectra (Figure 2e) clearly display the characteristic peaks for Pd in the 0 and +2 oxidation states.[13] In addition, the binding energy of the $3d_{5/2}$ electrons for high-spin Pd^0 is negatively shifted compared to that of traditional Pd^0, indicating that spin state modulation can reduce the electron escape work function. Combined with

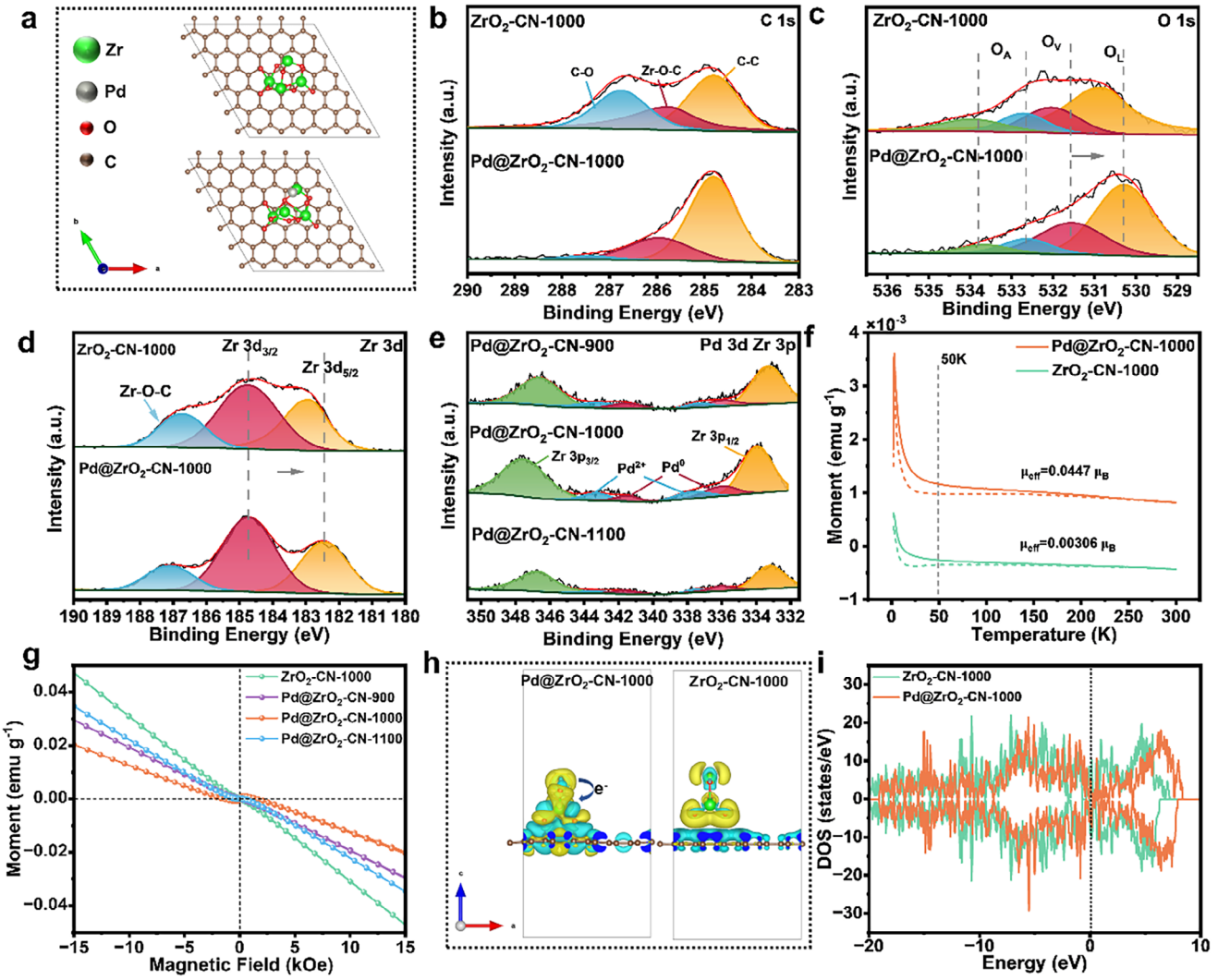

Figure 2. Structural characterizations of catalysts. a) Schematic diagram of the material structure. b) C 1s, c) O 1s and d) Zr 3d XPS spectra of ZrO_2-CN-1000 and Pd@ZrO_2-CN-1000. e) Pd 3d and Zr 3p XPS spectra of Pd@ZrO_2-CN-X (X = 900, 1000, 1100). f) Magnetic temperature (M-T) curves of ZrO_2-CN-1000 and Pd@ZrO_2-CN-1000. g) Magnetic hysteresis (M-H) curves of ZrO_2-CN-1000 and Pd@ZrO_2-CN-X (X = 900, 1000, 1100) at 300 K. h) The differential charge density and i) The TDOS of ZrO_2-CN-1000 and Pd@ZrO_2-CN-1000.

the ICP test results (Table S2, Supporting Information) and elemental content analysis (Table S3, Supporting Information), it is further confirmed that the relative content of +2 valence Pd ions is the highest in the Pd@ZrO_2-CN-1000 sample.

According to crystal field theory and electronic structure analysis, when Pd loses electrons and transitions from the 0 oxidation state to the +2 oxidation state, a half-filled configuration is formed in the e_g orbitals, resulting in a high-spin configuration (Figure S9, Supporting Information).[14] To verify this, we analyzed the trend of saturated magnetization with temperature. Figure 2f shows the magnetization-temperature (M-T) curves of the samples under field cooling (FC) and zero-field cooling (ZFC) conditions. It is evident that the magnetization of the Pd@ZrO_2-CN-1000 sample is higher than that of the ZrO_2-CN-1000 throughout the entire temperature range, particularly exhibiting a significantly enhanced magnetic response in the low-temperature region (<50 K). This indicates that the introduction of Pd significantly increases the number of unpaired d electrons, thereby enhancing paramagnetism. This can be attributed to the electronic structural adjustments in the d orbitals caused by the Pd loading, which enhance the local magnetic moment and increase the number of unpaired electrons.[15] In addition, the magnetization of both samples decreases with increasing temperature, exhibiting typical paramagnetic characteristics, further indicating that the magnetism arises from the thermal excitation of unpaired electrons. However, the Pd@ZrO_2-CN-1000 sample maintains a higher magnetization at elevated temperatures, suggesting that the magnetic states formed after Pd loading exhibit better thermal stability, which is closely related to the strong magnetic contribution provided by Pd. To validate this perspective more intuitively, the effective magnetic moment (μ_{eff}) was calculated from the linear fit of the χ^{-1} versus temperature (T) data. The results show that the magnetization (χ = M/H) of the samples follows the Curie–Weiss law. Further analysis indicates that

the number of unpaired electrons in the d orbitals (n) is positively correlated with the effective magnetic moment. Specifically, the calculated effective magnetic moments for Pd@ZrO_2-CN-1000 and ZrO_2-CN-1000 are 0.0447 μ_B and 0.00306 μ_B, respectively. This result indicates a significant increase in the number of unpaired d electrons in the sample after Pd loading. The M-H curves in Figure 2g show that the hysteresis loops of ZrO_2-CN-1000 and Pd@ZrO_2-CN-X (X = 900, 1000, 1100) exhibit a linear decreasing trend with no significant hysteresis phenomenon, reflecting their diamagnetic characteristics. Furthermore, the linear slope of Pd@ZrO_2-CN-1000 is lower than that of the other three samples, indicating that the introduction of Pd not only weakens the overall diamagnetism of the material but also reflects a relatively strong local spin magnetic moment. This phenomenon can be attributed to the fact that after Pd doping, Pd atoms lose some of their d orbital electrons due to electron transfer, thereby forming high-spin states with unpaired electron sites. These high-spin sites not only enhance the local magnetic moment but also exert a counteracting effect on the diamagnetism of the ZrO_2 lattice, leading to a reduction in overall diamagnetism. In other words, the addition of Pd triggers a competition between local spins and lattice diamagnetism, altering the macroscopic magnetic response of the material.

DFT calculation results further reveal the intrinsic mechanism behind this change and its optimization effects. The differential charge simulation (Figure 2h) indicates that the introduction of Pd triggers significant charge transfer from Pd to Zr in the hybrid structure, leading to an unbalanced charge distribution at the interface, which also explains the formation of high-spin state Pd. Charge density analysis (Figure 2i) shows that, compared to ZrO_2-CN-1000, the electronic state distribution of Pd@ZrO_2-CN-1000 expands from −20 to 10 eV, with an enhanced density of states peak near the Fermi level, indicating an enhancement in metallic character and resulting in improved conductivity. Additionally, the center of the d-band in Pd@ZrO_2-CN-1000 is lowered, which reduces the barrier for electron/ion transfer and facilitates easier electron excitation. These results indicate that the enhanced magnetism is primarily due to the increase in spin states, rather than surface oxidation effects. Moreover, the introduction of high-spin state Pd not only optimizes the electronic structure of the sample but also enhances its local magnetic moment and spin state distribution.

Through a series of characterizations, we further explored the electronic transfer capability and the optimization of surface/interface properties of the samples after loading with high-spin state Pd. The calculated results for the Fermi level indicate that the overall Fermi level of the material significantly shifts downward after Pd loading (**Figure 3a**), suggesting that Pd@ZrO_2-CN-1000 has higher electron affinity, thus exhibiting stronger electron transfer capability. The calculation of the work function further supports this conclusion (Figure 3b,c), showing that the interface barrier depth of Pd@ZrO_2-CN-1000 is relatively smaller compared to ZrO_2-CN-1000, indicating that the electron escape work of this material is relatively lower. To intuitively verify the changes in the material's conductivity, we measured the intrinsic resistance of both samples using the four-probe method (Figure 3d). The results show that the resistivity of Pd@ZrO_2-CN-1000 is lower than that of ZrO_2-CN-1000, further confirming the enhancement of electronic conductivity. The valence band spectrum test results also indicate (Figure 3e; Figure S26, Supporting Information) that the band structure of the sample was significantly optimized after the introduction of Pd. The valence band maximum of Pd@ZrO_2-CN-1000 shifts downward by 0.35 eV relative to the Fermi level, suggesting that the introduction of Pd enhances electronic conductivity. Furthermore, compared to ZrO_2-CN-1000, the valence band width of Pd@ZrO_2-CN-1000 significantly increases, indicating a broader electronic state distribution range, which is consistent with the conclusions from theoretical simulations. In addition, by fitting the valence band spectrum, we assessed the d-band center positions of the two samples (Figure 3f). Compared to ZrO_2-CN-1000, the d-band center of Pd@ZrO_2-CN-1000 shifts upward by 0.59 eV, indicating that the introduction of Pd enhances the adsorption strength of surface ions.

To further investigate the optimization of interfacial interactions, the surface potentials of ZrO_2-CN-1000 and Pd@ZrO_2-CN-1000 were compared through Zeta potential measurements (Figure 3g). The results indicate that the Zeta potential has shifted positively. Further analysis shows that the loading of Pd leads to a redistribution of surface charges, creating a localized high-spin environment rich in electrons. Combined with XPS analysis (Figure 2c,d), we found that the electron transfer from Pd to Zr and O enhances the Lewis acidity of the Pd sites, thereby increasing the surface positive charge density. This change in charge state directly promotes the adsorption of OH^- in the electrolyte, providing more active sites for the redox reaction. Additionally, compared to ZrO_2-CN-1000 (Figure 3h), the contact angle on the surface of Pd@ZrO_2-CN-1000 (Figure 3i) is significantly reduced, indicating better wettability, which also facilitates the rapid diffusion of electrolyte ions.

To demonstrate the impact of high-spin state Pd loading on electrochemical energy storage activity, we evaluated the electrochemical performance of ZrO_2-CN-1000 and Pd@ZrO_2-CN-X (X = 900, 1000, and 1100) in a three-electrode cell containing 6 M KOH electrolyte. **Figure 4a** shows that both ZrO_2-CN-1000 and Pd@ZrO_2-CN-X exhibit distinct redox peaks in their cyclic voltammetry (CV) curves, attributed to the Faradaic reactions of Pd^0/Pd^{2+} and Zr^{2+}/Zr^{3+}. At the same scan rate, the Pd@ZrO_2-CN-1000 electrode demonstrates higher redox peaks and a larger CV curve area, indicating stronger energy storage capacity.[16] Figure 4b shows that both ZrO_2-CN-1000 and Pd@ZrO_2-CN-X (X = 900, 1000, and 1100) exhibit nonlinear constant current charge–discharge (GCD) curves, with Pd@ZrO_2-CN-1000 demonstrating the longest discharge time, which is consistent with the conclusions drawn from the CV curves. In Figure 4c, the CV curves of the Pd@ZrO_2-CN-1000 electrode indicate that as the scan rate increases, the peak currents for both the cathodic and anodic processes enhance.[17] At the same time, the peak positions exhibit slight shifts due to polarization at higher scan rates. The GCD curves of Pd@ZrO_2-CN-1000 at different current densities (Figure S10, Supporting Information) show nearly symmetrical charge–discharge profiles, indicating its excellent coulombic efficiency and reversible redox capacitance.[18] The comparative analysis of specific capacitance for ZrO_2-CN-1000 and Pd@ZrO_2-CN-X at different current densities is shown in Figure 4d. Pd@ZrO_2-CN-1000 reached 773.3 F g^{-1} at 1 A g^{-1}, outperforming other Pd-based energy storage materials (Figure 4e; Table S4, Supporting Information). Through fitting,

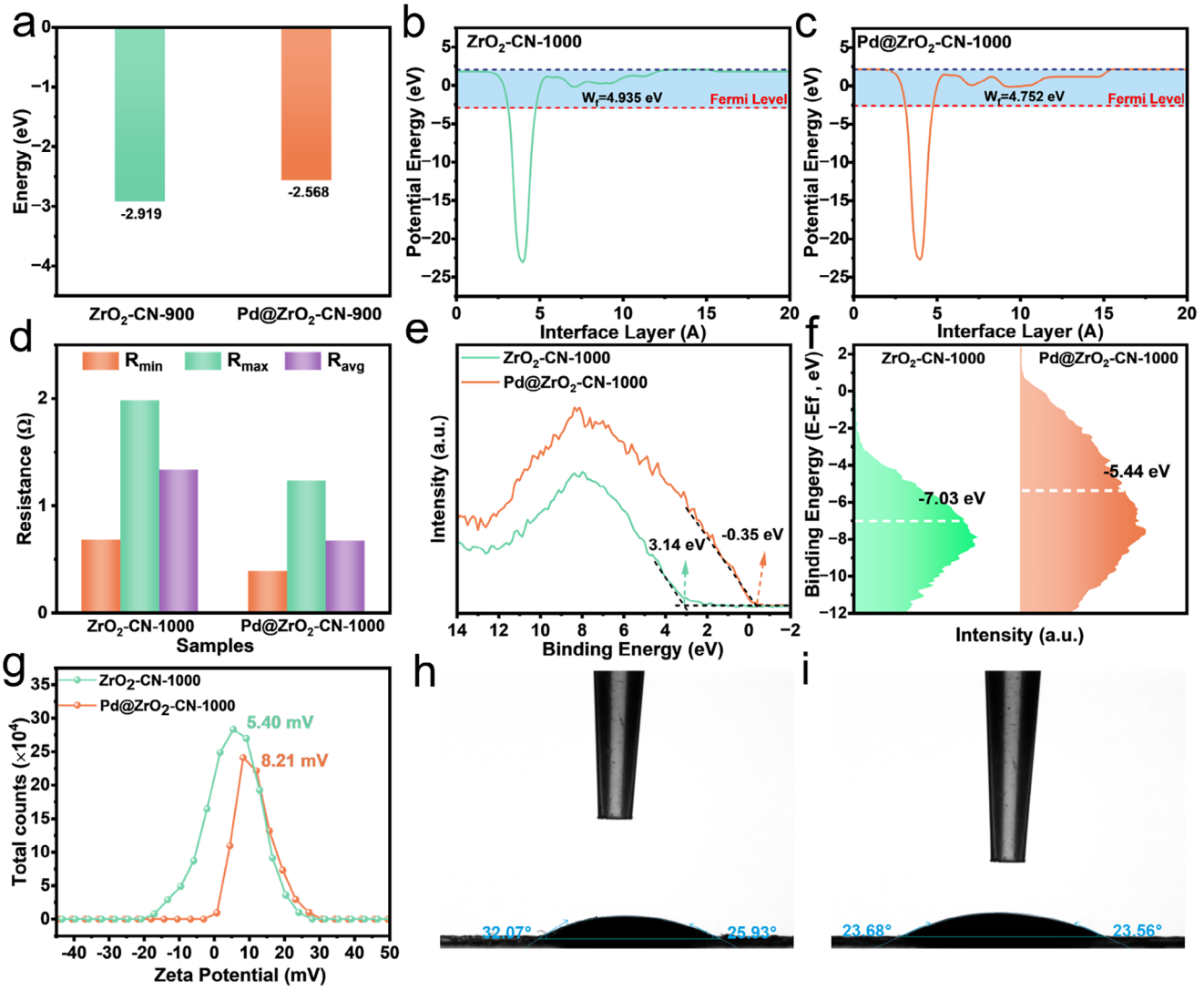

Figure 3. Surface and interfacial characteristics of catalysts. a) The Fermi level image of ZrO_2-CN-1000 and Pd@ZrO_2-CN-1000. The work function image of b) ZrO_2-CN-1000 and c) Pd@ZrO_2-CN-1000. d) Resistivity features, e) Valence band spectra, f) The d-band centers based on the fitting of the band structure spectrum, and g) Zeta potentials images of ZrO_2-CN-1000 and Pd@ZrO_2-CN-1000. Contact angle images of h) ZrO_2-CN-1000 and i) Pd@ZrO_2-CN-1000.

Pd@ZrO_2-CN-1000 still maintained excellent rate performance with a capacitance of 692.5 F g^{-1} at a current density of 10 A g^{-1}.

The charge transfer and diffusion behaviors of different electrodes were investigated in depth using electrochemical impedance spectroscopy (EIS) (Figure 4f). The values of series resistance (R_s) and charge transfer resistance (R_{ct}) for ZrO_2-CN-1000 and Pd@ZrO_2-CN-X (X = 900, 1000, and 1100) are provided in Table S5 (Supporting Information). Compared to ZrO_2-CN-1000, the Pd@ZrO_2-CN-X (X = 900, 1000, and 1100) electrode exhibits the lowest intrinsic resistance and charge transfer impedance, indicating that the intrinsic resistance of the electrodes is reduced after the introduction of Pd.[19] This change is positively correlated with the shift in the d-band center and the change in the Fermi level. To further verify the changes in electrochemical kinetics after the introduction of Pd, the trend of imaginary part capacitance (C″) with respect to frequency was analyzed (Figure 4g). In the low-frequency region, the C″ value of Pd@ZrO_2-CN-1000 is significantly higher than that of ZrO_2-CN-1000, indicating that it has a greater ionic charge storage capacity at low frequencies, which can be attributed to the enhanced double-layer effect after Pd modification. As the frequency increases, the C″ values for both samples gradually decrease and stabilize in the high-frequency region. The C″ of Pd@ZrO_2-CN-1000 remains at a relatively high level across a wide frequency range, demonstrating its superior electrochemical response in the high-frequency region compared to ZrO_2-CN-1000.[20] Additionally, Pd@ZrO_2-CN-1000 exhibits a significant C″ peak near the low-frequency region, indicating that it has a shorter relaxation time constant and a faster electrochemical reaction rate. A comparison of the Warburg impedance slopes further confirms that Pd@ZrO_2-CN-1000 has the lowest diffusion resistance (Figure S11, Supporting Information).[21] Analysis of the phase

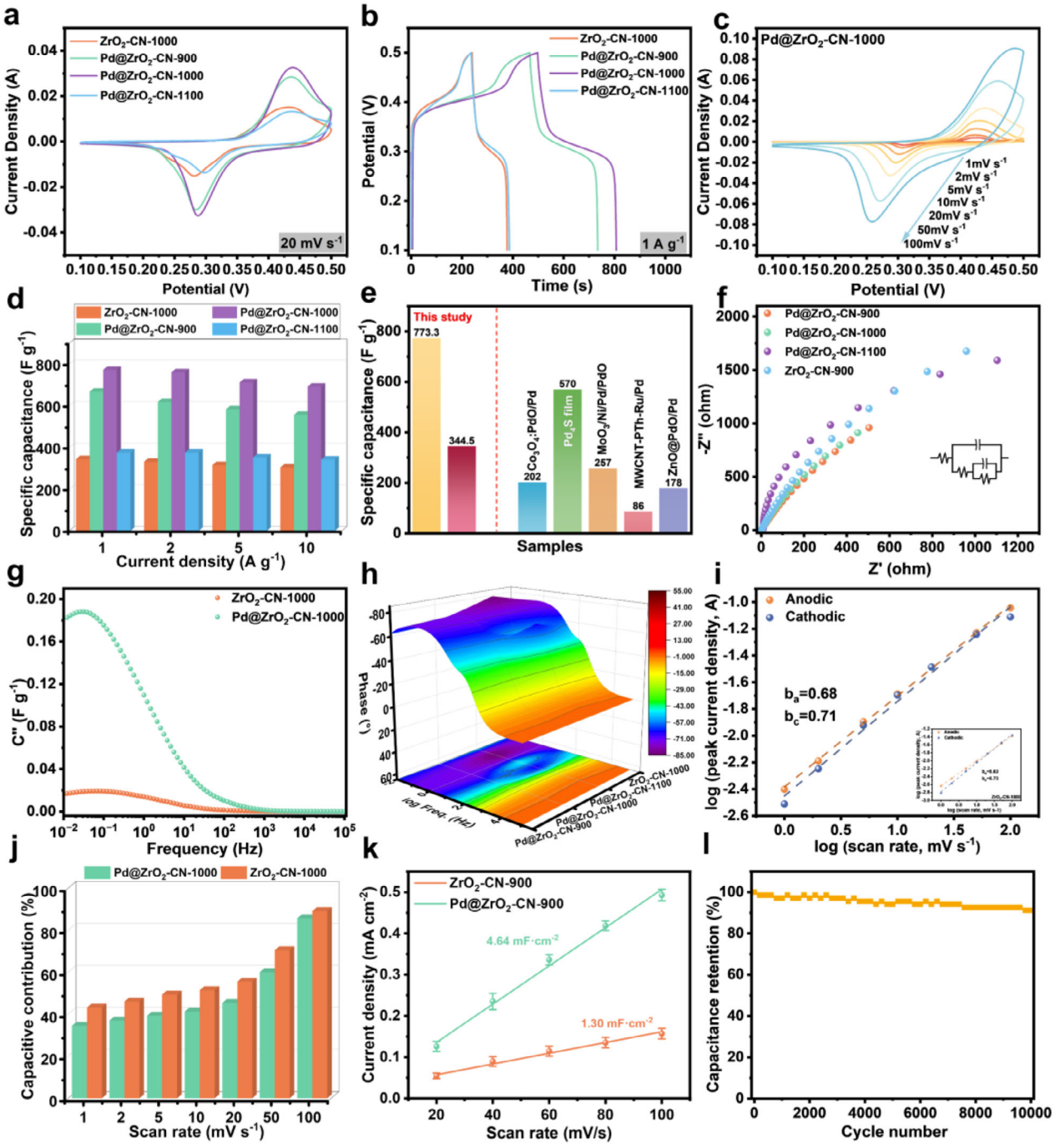

Figure 4. Electrochemical activity and mechanism testing. Comparison of a) CV curves, and b) GCD profiles at different current densities of ZrO_2-CN-1000 and Pd@ZrO_2-CN-X ($X = 900, 1000, 1100$). c) CV curves at different scan rates of Pd@ZrO_2-CN-1000. d) Specific capacitances at different current densities of ZrO_2-CN-1000 and Pd@ZrO_2-CN-X ($X = 900, 1000, 1100$). e) Comparison of the mass-specific capacitance of Pd@ZrO_2-CN-1000 and other electrodes. f) EIS Nyquist plots of several samples. g) The imaginary capacitance versus frequency curves for ZrO_2-CN-1000 and Pd@ZrO_2-CN-1000. h) Bode plots of several samples. i) Calculation of power law exponents, j) Capacitance contribution ratio histograms, and k) C_{dl} values of ZrO_2-CN-1000 and Pd@ZrO_2-CN-1000. l) Cyclic stability for 10 000 cycles at 10 A g^{-1} of Pd@ZrO_2-CN-1000.

angle variation across different frequency ranges (Figure 4h) shows that the phase angle of ZrO_2-CN-1000 changes relatively smoothly with frequency, whereas after loading with Pd, the phase angle of the sample significantly increases in the low-frequency region. This indicates that the Pd loading enhances the frequency response characteristics and improves the material's ability to adsorb and react with OH^- on the surface (Figures S12, S13, Supporting Information).[22]

To clarify the impact of high-spin state Pd loading on the energy storage mechanism, the charge storage mechanisms of the

ZrO_2-CN-1000 and Pd@ZrO_2-CN-1000 electrodes were investigated using CV curves (Figure 4i).[23] The b value is calculated using Equation (1), as follows:

$$i = av^b \quad (1)$$

where i represents the peak current, v is the scan rate, and a and b are constants.

When $b \leq 0.5$, the energy storage mechanism is diffusion-controlled, while $b = 1$ indicates a surface capacitance-controlled energy storage mechanism.[24] The b values for ZrO_2-CN-1000 and Pd@ZrO_2-CN-1000 are 0.62 and 0.66, respectively (Figure 4i), falling between 0.5 and 1. This indicates that both electrodes exhibit characteristics of both diffusion-controlled and capacitance-controlled mechanisms, with Pd@ZrO_2-CN-1000 having a greater proportion of diffusion control.

The contribution rates of these two behaviors are calculated using Equation (2), as follows[25]:

$$i = k_1 v + k_2 v^{1/2} \quad (2)$$

where $k_1 v$ and $k_2 v^{1/2}$ represent the capacitive and diffusion contributions, respectively.

Figure 4j shows that as the scan rate increases, the capacitive effects of the ZrO_2-CN-1000 and Pd@ZrO_2-CN-1000 electrodes are enhanced, primarily due to the limitation of the reaction time between electrons and the active materials, which strengthens the surface-limited capacitance. Interestingly, the diffusion control ratio of Pd@ZrO_2-CN-1000 is higher than that of ZrO_2-CN-1000 at all scan rates, indicating that the loading of high-spin state Pd promotes the intercalation of OH^-, allowing it to store more ions and thereby improving electrochemical performance (Figures S14, S15, Supporting Information). The electrochemical active surface area (ECSA) was confirmed by calculating the double-layer capacitance (C_{dl}).[26] Figure 4k shows that the active areas of ZrO_2-CN-1000 and Pd@ZrO_2-CN-1000 are similar. Combined with the BET test results, this indicates that the contribution of morphological changes to the enhancement of capacitance is limited, thereby ruling out the possibility that the improved electrochemical performance is due to an increase in surface area. The performance enhancement is primarily attributed to the electronic effects induced by the high-spin state (Figure S16, Supporting Information). The initial data on the specific surface area and porosity of the electrode materials also indicate that changes in specific surface area are not the main reason for the increased activity of the electrode materials; this enhancement should be attributed to the improved efficiency of the energy storage active sites (Figure S4 and Table S1, Supporting Information). Cycle stability is crucial for the practical application of electrode materials. The Pd@ZrO_2-CN-1000 electrode retains 91.2% of its capacitance after 10 000 cycles at a current density of 10 A g^{-1}, demonstrating excellent cycling stability. The crystal structure and macroscopic morphology of the samples after cycling did not show significant changes, which also confirms the source of their high cycling stability (Figure S17, Supporting Information).

Based on the evidence from the electrochemical kinetics and energy storage mechanisms described above, high-spin state Pd enhances electrochemical energy storage activity by optimizing the adsorption of intermediates and the efficiency of electron conduction. First, the unpaired electrons of Pd increase the width of its d orbital electron density, facilitating strong interactions with the OH^- orbitals. Second, the adsorption of OH^- relies on the coordination bonds between the metal and oxygen atoms, and the electronic cloud shape of high-spin state Pd is better suited to provide appropriate feedback electrons, thereby enhancing adsorption capacity. Finally, the splitting of d electron energy levels brings some levels closer to the Fermi level, and the high density of electronic states near the Fermi level improves conductivity. Thus, the loading of high-spin state Pd can effectively enhance the rate of Faradaic reactions, enabling rapid and efficient energy storage.

Through a series of spectral analyses and first-principles density functional theory (DFT) calculations, the fundamental reason for the enhanced energy storage activity of high-spin state Pd sites has been revealed. DFT calculations indicate that there are differences in the adsorption energies of OH^- on surface Zr and Pd sites. As shown in **Figure 5a**, the enhancement of the electropositivity of Pd increases its Lewis acidity, thereby strengthening its interaction with the electron-rich OH^- intermediates. This is reflected in the higher adsorption energy at the Pd sites compared to the Zr sites, indicating that the loading of high-spin state Pd significantly enhances the adsorption capacity of OH^-, facilitating the adsorption of more OH^- on the surface and thus improving the efficiency of energy storage reactions. The Py-IR spectra of ZrO_2-CN-1000 and Pd@ZrO_2-CN-1000 both display characteristic adsorption peaks in the range of 1400–1650 cm^{-1}. The peaks at 1450, 1577, and 1613 cm^{-1} are attributed to the chemical adsorption of pyridine at the surface Lewis acid sites (L), while the peaks at 1540 and 1638 cm^{-1} indicate the presence of Brønsted acid sites (B).[27] The signal at 1494 cm^{-1} reflects the combined contributions of Lewis acid and Brønsted acid sites (Figure 5b; Figure S21, Supporting Information). Notably, after loading with Pd, the concentration of surface Lewis acid sites in the sample significantly increases. The Lewis acid site density, calculated by integrating the peak areas, is 1.25 times higher than that of ZrO_2-CN-1000, indicating the presence of uncoordinated or weakly coordinated metal centers. These centers are prone to attack by electron donor lone pairs, leading to strong interactions that enhance the intensity of energy storage reactions (Table S7, Supporting Information). The NH_3-TPD test results further support this viewpoint. Figure 5c shows the ammonia desorption behavior of ZrO_2-CN-1000 and Pd@ZrO_2-CN-1000 samples. ZrO_2-CN-1000 exhibits only a gentle desorption curve with no significant desorption peaks, indicating a low density of acidic sites. In contrast, Pd@ZrO_2-CN-1000 displays three distinct desorption peaks at 111, 230, and 300 °C, corresponding to weak acidity, medium acidity, and strong acidity sites, respectively.[28] This indicates that the loading of Pd effectively enhances the surface acidity, promoting the adsorption of OH^-.

To validate the enhancement of energy storage kinetics by surface high-spin sites, in-situ Raman spectroscopy was employed to study the real-time energy storage process. As shown in Figure 5d,e, the ZrO_2-CN-1000 and Pd@ZrO_2-CN-1000 samples exhibited distinct Raman characteristic peaks at different potentials. In the ZrO_2-CN-1000 sample (Figure 5d), with increasing potential, the main observed vibrational modes were M (≈200 cm^{-1}), B_{1g} (≈320 cm^{-1}), and E_g (≈460 cm^{-1}), which are attributed to the lattice vibrations of ZrO_2. However, the vibrational

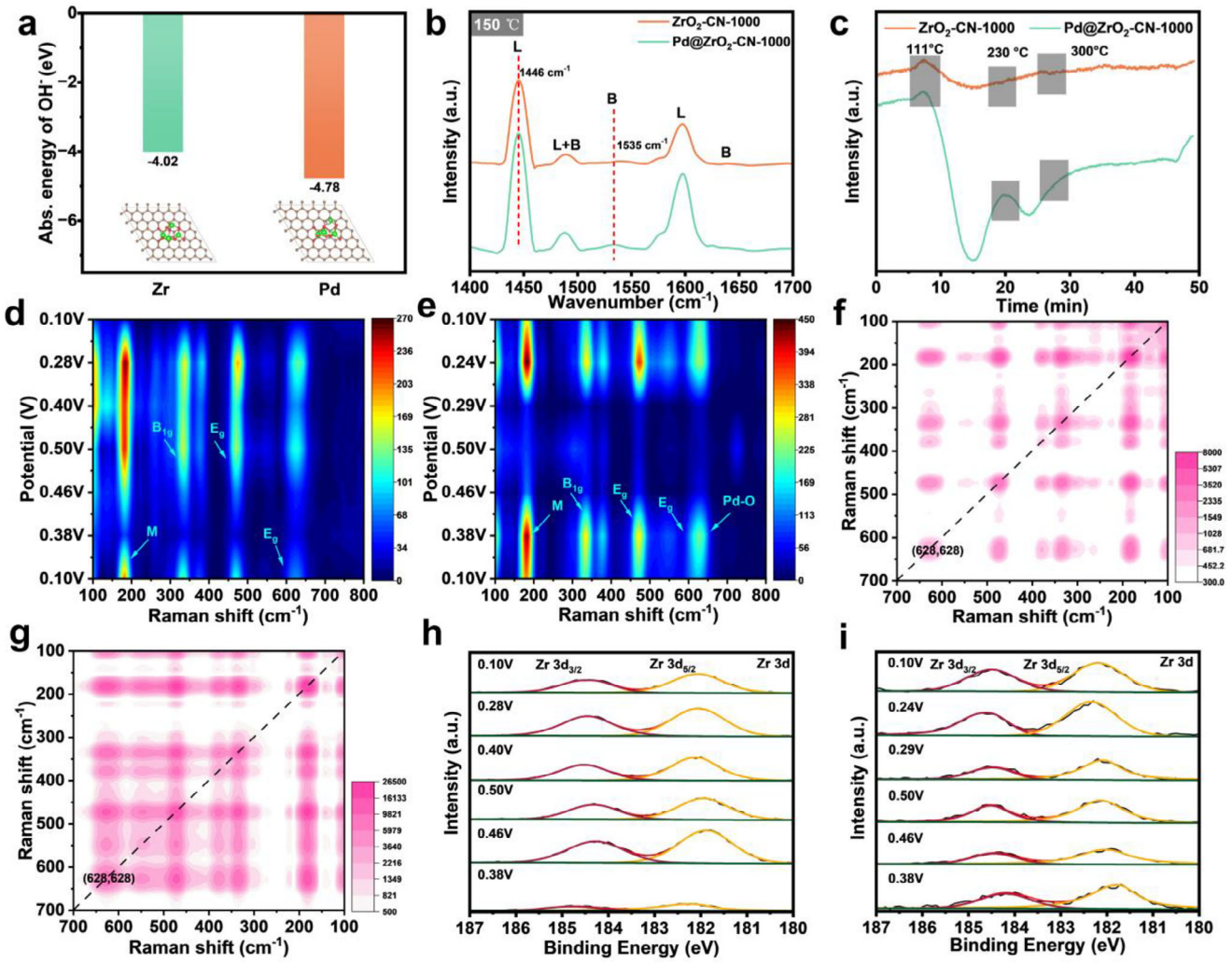

Figure 5. Multiple high-resolution spectroscopy characterizations tracing energy storage evolution process of localized high-spin states in palladium. a) The adsorption energies of OH^- in Zr and Pd. b) Py-IR spectra, and c) H_2-TPR curves of ZrO_2-CN-1000 and Pd@ZrO_2-CN-1000. d) In situ Raman of ZrO_2-CN-1000 and e) Pd@ZrO_2-CN-1000. Synchronized 2D-CORS mappings of f) ZrO_2-CN-1000 and g) Pd@ZrO_2-CN-1000. XPS spectra of Zr 3d for h) ZrO_2-CN-1000 and i) Pd@ZrO_2-CN-1000 at different potentials.

intensity of the peaks varied relatively weakly with potential, indicating a lower intensity of surface reactions. In contrast, in the Pd@ZrO_2-CN-1000 sample, in addition to the ZrO_2 lattice vibrational modes, a significant Pd—O vibrational peak appeared at ≈700 cm^{-1}, indicating that the introduction of Pd-induced new vibrational modes (Figure 5e). This is closely related to the strong interaction between Pd and OH^- and suggests that the introduction of high-spin state Pd facilitates the generation of reactive species during the redox process. Furthermore, all peak intensities in the Pd@ZrO_2-CN-1000 sample at high potentials were significantly enhanced, especially the Pd—O peak, further confirming that the introduction of Pd improved the electrochemical activity during the energy storage process. The synchronous 2D correlation Raman spectroscopy (2D-CORS) further corroborated the enhancement of the kinetic process.[29] In Figure 5f,g, the synchronous spectra of ZrO_2-CN-1000 and Pd@ZrO_2-CN-1000 samples exhibit different energy storage behaviors. For ZrO_2-CN-1000 (Figure 5f), a significant self-peak appears at ≈628 cm^{-1}, attributed to the lattice vibrational modes of ZrO_2. The intensity of the self-peak is weak, and the distribution of orthogonal cross-peaks is sparse, indicating a limited dynamic range of reactive species and fewer active sites. In contrast, the self-peak intensity at ≈628 cm^{-1} in Pd@ZrO_2-CN-1000 is significantly enhanced, with a denser distribution of orthogonal cross-peaks, especially in the low wavenumber region (≈100–300 cm^{-1}) and high wavenumber region (≈600–700 cm^{-1}), indicating that the introduction of Pd significantly promotes the synergistic changes of different vibrational modes during the energy storage process. Additionally, we collected Zr 3d and Pd 3d XPS spectra at different potentials to monitor the changes in the near-surface electronic structure of the materials and clarify the roles of Pd and Zr in the energy storage mechanism. The time-evolution XPS spectra of Pd at different potentials (Figure S22, Supporting Information) show that the Pd 3d signal exhibits a reversible transformation between Pd^0 and Pd^{2+}, indicating that Pd acts as an active center during the energy storage process, further

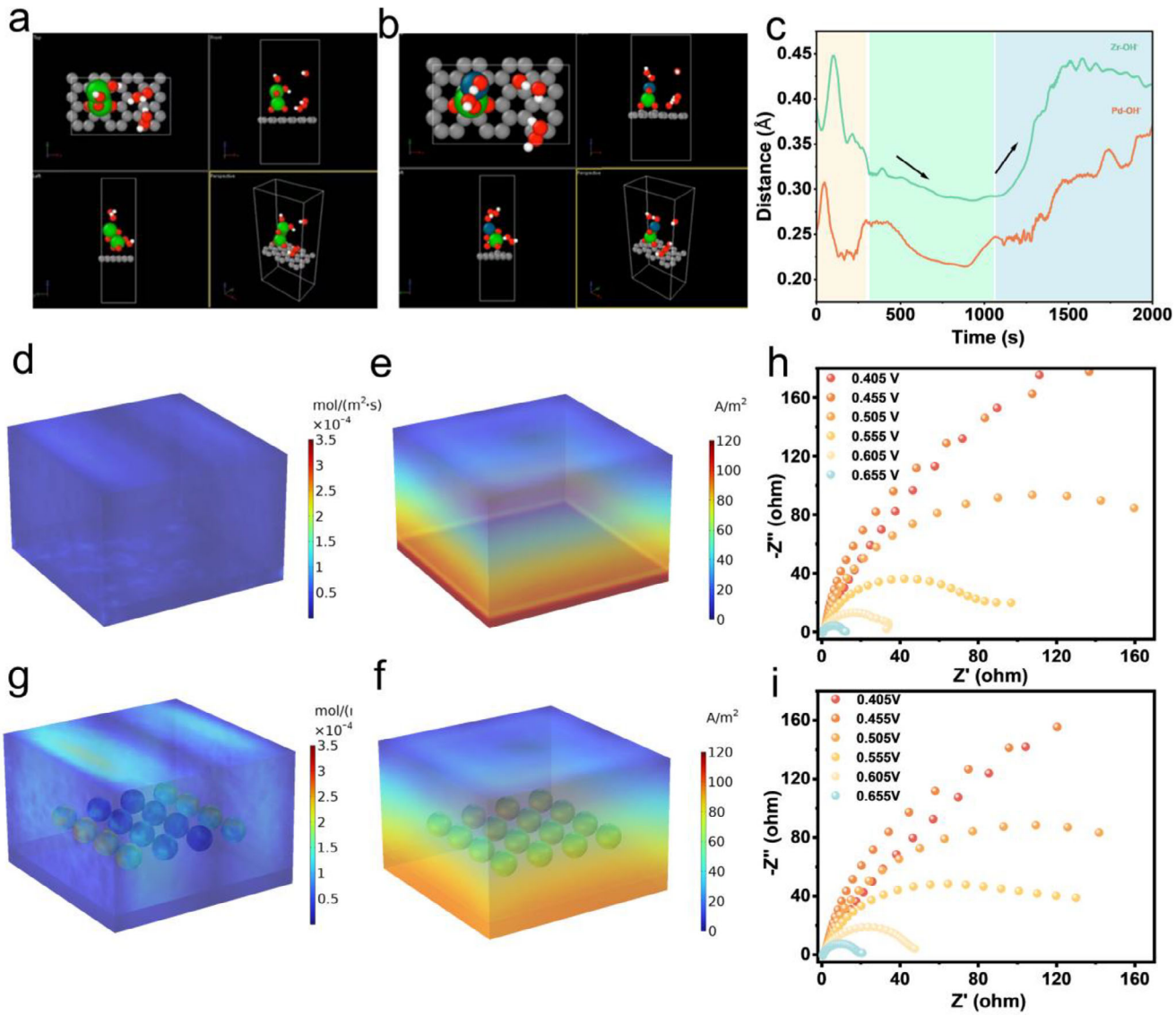

Figure 6. Kinetic calculations and multiphysics simulations for optimizing energy storage dynamics. Molecular dynamics simulation models of a) ZrO_2-CN-1000 and b) Pd@ZrO_2-CN-1000. c) Molecular dynamics simulation models of ZrO_2-CN-1000 and Pd@ZrO_2-CN-1000. COMSOL simulation results of the electrolyte ion flux for d) ZrO_2-CN-1000 and e) Pd@ZrO_2-CN-1000 electrodes after 10 s of reaction. COMSOL simulation results of the current density for f) ZrO_2-CN-1000 and g) Pd@ZrO_2-CN-1000 electrodes after 10 s of reaction. Nyquist plots of h) ZrO_2-CN-1000 and i) Pd@ZrO_2-CN-1000 at different applied potentials.

enhancing electron transfer efficiency. Figure 5h shows that the binding energies of Zr $3d_{5/2}$ and Zr $3d_{3/2}$ in ZrO_2-CN-1000 only exhibit a slight shift with increasing potential, indicating that Zr does not significantly participate in electron transfer reactions during the energy storage process, resulting in a relatively stable electronic structure and limited reaction activity. In contrast, in the Pd@ZrO_2-CN-1000 sample (Figure 5i), the binding energies of Zr $3d_{5/2}$ and Zr $3d_{3/2}$ shift significantly toward lower energy as the potential increases, suggesting that the introduction of Pd significantly regulates the electronic structure, enabling it to participate more actively in redox reactions during the energy storage process. This change in binding energy indicates that the presence of Pd facilitates the adsorption of OH^- and electron transfer.[30]

Based on the above results, we performed molecular dynamics simulations of the energy storage processes for ZrO_2-CN-1000 and Pd@ZrO_2-CN-1000 (**Figure 6**a,b). In this process, the relative positions of surface elements and OH^- were described using the curves of the center of mass distances (CoMs) versus reaction time. As shown in Figure 6c, the dynamic changes in the relative center distances of Zr-OH^- and Pd-OH^- during the charging and discharging processes were illustrated to reveal the cooperative mechanism of Pd and Zr in the energy storage process. In the initial charging stage (0–500 s), the distance of Pd-OH^- rapidly decreased, while the distance of Zr-OH^- also decreased but at a slower rate, indicating that OH^- preferentially adsorbed onto the Pd surface, meaning that Pd served as the main active site during this stage. Subsequently, in the continued charging process

(500–1000 s), ions began to diffuse into the lattice, the distance of Pd-OH^- gradually stabilized, while the distance of Zr-OH^- further decreased, suggesting that some OH^- diffused from Pd to Zr, indicating that Zr gradually participated in the reaction. During the discharging stage (1000–2000 s), the distance of Zr-OH^- significantly increased, while the distance of Pd-OH^- fluctuated, indicating that OH^- gradually desorbed from the Zr surface and redistributed onto the Pd surface during the discharging process, completing the full cycle of the charging and discharging reaction (Movies S1 and S2, Supporting Information). Overall, this process demonstrates that Pd plays a crucial role in regulating the adsorption of OH^-, facilitating the migration and stabilization of intermediate species, and enhancing the reversibility of the reaction, thereby promoting an efficient reaction pathway for the charging and discharging processes. Although short-term simulations cannot fully capture long-term dynamics, their results are consistent with the experimentally observed rapid adsorption enhancement phenomena (such as in situ Raman spectroscopy and electrochemical kinetic analyses), confirming that the simulation parameters effectively reveal the characteristics of interfacial reactions.

COMSOL simulations were employed to understand the fundamental reasons behind the accelerated energy storage reaction kinetics due to the modulation of the high-spin surface microenvironment at the mesoscopic scale. The electrolyte current density serves as an indicator to measure the magnitude and direction of the current caused by ion migration, effectively reflecting the interactions between the electrode and the electrolyte. Dynamic concentration gradient changes were not considered in the simulations; however, a constant electrolyte concentration assumption was made to remain consistent with the experimental static testing conditions. Figure 6d,e compare the electrolyte current density distributions of ZrO_2-CN-1000 and Pd@ZrO_2-CN-1000 after 10 s of reaction on the electrode. The changes in the spin states at the electrode surface lead to variations in local exchange current density and reaction rate, indicating a stronger binding ability with electrolyte ions and a faster charge transfer rate. This results in a significant enhancement of the near-surface electrolyte current density (Figure 6f,g) and electric field strength (Figure S23, Supporting Information) for both ZrO_2-CN-1000 and Pd@ZrO_2-CN-1000. At the same interface position, the current density (79.62 A m^{-2}) and ion concentration (1.54 mol $(m^2 \cdot s)^{-1}$) of Pd@ZrO_2-CN-1000 are significantly higher than those of ZrO_2-CN-1000 (72.06 A m^{-2} and 0.52 mol $(m^2 \cdot s)^{-1}$), which is highly consistent with the conclusion of reduced charge transfer resistance observed in experiments. Furthermore, the increase in ion concentration of Pd@ZrO_2-CN-1000 indicates a significant enhancement in its interfacial OH^- adsorption and migration capabilities, aligning with the conclusion drawn from Zeta potential and contact angle measurements regarding optimized surface hydrophilicity. These results collectively validate that high-spin state Pd accelerates charge transfer and ion diffusion by optimizing the electronic structure and interfacial microenvironment. In Figure 6h,i, the in situ Nyquist plots for ZrO_2-CN-1000 and Pd@ZrO_2-CN-1000 visually demonstrate the impedance characteristics and changes in adsorption strength at different potentials. The introduction of Pd significantly optimizes ion transfer and interfacial processes during the energy storage process. In the higher frequency region, the reduction of the arc segment is associated with the enhancement of the double-layer capacitance, indicating that the incorporation of Pd lowers the interfacial impedance and improves ion diffusion behavior. In the lower frequency region, the curves approach a vertical line, reflecting the superior pseudocapacitance characteristics and charge storage capacity of the Pd@ZrO_2-CN-1000 sample. Furthermore, compared to ZrO_2-CN-1000, the Pd@ZrO_2-CN-1000 exhibits a lower charge transfer resistance (R_{ct}) under the same applied potential, which is attributed to the enhanced affinity for OH^- due to the introduction of Pd. It is worth noting that if the modulation of the active sites leads to excessively strong binding with the intermediates, it could result in kinetic hindrances, manifested as a slowdown in ion desorption, thereby significantly reducing discharge performance.

3. Conclusion

In summary, this study successfully constructed a local high-spin environment by modifying high-spin configured Pd nanoparticles on the surface of NH_2-UiO-66 derivatives, systematically revealing their role in enhancing energy storage activity. The combination of theoretical calculations, in situ spectroscopy, and multi-scale dynamic analysis indicates that the introduction of high-spin state Pd creates an enhanced Lewis acidic environment rich in weakly coordinated metal centers on the electrode surface, significantly improving the adsorption capacity and reactivity of electron-rich intermediates. Meanwhile, the spin polarization effect increases the delocalization of d electrons and generates new electronic states near the Fermi level, thereby accelerating electron transfer and enhancing the efficiency of electrochemical reaction kinetics. Thanks to this mechanism, the constructed Pd@ZrO_2-CN-1000 electrode exhibits a higher proportion of diffusion control, demonstrating outstanding energy storage performance (773.3 F g^{-1} at 1 A g^{-1}) and good cycling stability. The electrode material design strategy based on optimizing the surface local spin environment, along with the combination of various spectroscopic characterizations and multi-scale modeling methods, provides a valuable approach for the targeted design and development of high-activity energy storage electrodes.

Supporting Information

Supporting Information is available from the Wiley Online Library or from the author.

Acknowledgements

X.L. and Y.Y. contributed equally to this work. This work was supported by the National Natural Science Foundation of China (No. 51073067). The authors also thank Shanghai Bojun Zhizhi Technology Service Co., Ltd. for providing partial experimental equipment and technical support.

Conflict of Interest

The authors declare no conflict of interest.

Data Availability Statement

The data that support the findings of this study are available from the corresponding author upon reasonable request.

Keywords

localized spin environment, palladium, redox kinetics, supercapacitors

Received: February 6, 2025
Revised: April 10, 2025
Published online: April 30, 2025

[1] a) J. Xu, X. Gong, Z. Meng, P. Chen, H. Nan, Y. Li, T. Deng, D. Wang, Y. Zeng, X. Hu, H. Tian, Z. Niu, W. Zheng, *Adv. Mater.* **2024**, *36*, 2401452; b) L. Q. Bai, Z. H. Hu, C. Hu, S. G. Zhang, Y. R. Ying, Y. G. Zhang, L. Li, H. F. Zhang, N. Li, S. S. Shi, S. Liu, L. Hao, T. Y. Liu, H. W. Huang, H. T. Huang, Y. H. Zhang, *Angew. Chem., Int. Ed.* **2023**, *62*, 2301631; c) S. Yang, H. M. Lv, Y. B. Wang, X. Guo, L. Z. Zhao, H. F. Li, C. Y. Zhi, *Angew. Chem., Int. Ed.* **2022**, *61*, 2209794; d) H. Fu, S. Huang, T. Wang, J. Lu, P. Xiong, K. Yao, J. S. Byun, W. Li, Y. Kim, H. S. Park, *Adv. Mater.* **2025**, *37*, 2411686.

[2] a) Q. Wang, B. Mao, S. I. Stoliarov, J. Sun, *Prog. Energy Combust. Sci.* **2019**, *73*, 95; b) R. Zhang, Z. Xu, Z. Hao, Z. Meng, X. Hao, H. Tian, *Carbon Energy* **2024**, *7*, 630; c) P. Xiong, Y. Kang, H. Yuan, Q. Liu, S. H. Baek, J. M. Park, Q. Dou, X. Han, W.-S. Jang, S. J. Kwon, Y.-M. Kim, W. Li, H. S. Park, *Appl. Phys. Rev.* **2022**, *9*, 011401.

[3] a) P. E. Lokhande, U. S. Chavan, A. Pandey, *Electrochem. Energy Rev.* **2020**, *3*, 155; b) K. Yang, H. Fu, Y. Duan, Z. Ma, D. Wang, B. Li, H. S. Park, D. Ho, *ACS Energy Lett.* **2024**, *9*, 209; c) S. Huang, P. Zhang, J. Lu, J. S. Kim, D. H. Min, J. S. Byun, M. J. Kim, H. Fu, P. Xiong, P. J. Yoo, W. Li, X. Yu, X. Qin, H. S. Park, *Energy Environ. Sci.* **2024**, *17*, 7870.

[4] C. Choi, D. S. Ashby, D. M. Butts, R. H. DeBlock, Q. L. Wei, J. Lau, B. Dunn, *Nat. Rev. Mater.* **2020**, *5*, 5.

[5] a) R. Farma, R. R. Hasibuan, A. Awitdrus, Y. Hamzah, E. Taer, A. Apriwandi, *J. Ovonic Res.* **2021**, *17*, 185; b) R. Rani, A. Kumar, M. Sharma, B. Mohan, R. Kumar, R. Chandra, V. K. Malik, *J. Phys. Chem. Solids* **2025**, *197*, 112428; c) A. P. Cohn, W. R. Erwin, K. Share, L. Oakes, A. S. Westover, R. E. Carter, R. Bardhan, C. L. Pint, *Nano Lett.* **2015**, *15*, 2727.

[6] a) S. Gumrukcu, E. Kaplan, M. B. Arvas, N. Kocyigit, M. Ozcesmeci, Y. Sahin, I. Ozcesmeci, *Energy Technol.* **2024**, 2400915; b) P. M. Anjana, M. R. Bindhu, M. Umadevi, R. B. Rakhi, *Appl. Surf. Sci.* **2019**, *479*, 96.

[7] a) Y. Wan, T. Cao, Y. Li, B. Wang, W. Wang, Y. Xu, H. Yang, D. Zhang, D. Zhang, Q. Li, C. Yu, H. Hu, M. Wu, *Adv. Funct. Mater.* **2024**, *3*, 34; b) P. L. Yadav, A. R. Shelke, H. T. Wang, K. H. Chen, W. X. Lin, C. W. Li, M. Y. Chen, P. H. Yeh, C. L. Dong, M. Qorbani, Y. C. Huang, J. W. Chiou, H. M. Tsai, P. M. Kadam, K. H. Chen, L. C. Chen, W. F. Pong, *ACS Appl. Energy Mater.* **2023**, *6*, 6443; c) X. Q. Wei, S. J. Song, W. W. Cai, X. Luo, L. Jiao, Q. Fang, X. S. Wang, N. N. Wu, Z. Luo, H. J. Wang, Z. H. Zhu, J. Li, L. R. Zheng, W. L. Gu, W. Y. Song, S. J. Guo, C. Z. Zhu, *Chem* **2023**, *9*, 181.

[8] a) C. Wang, P. Zhai, M. Xia, W. Liu, J. Gao, L. Sun, J. Hou, *Adv. Mater.* **2023**, *35*, 2209307; b) H. Ding, H. Liu, W. Chu, C. Wu, Y. Xie, *Chem. Rev.* **2021**, *121*, 13174.

[9] J. Batista, A. Pintar, D. Mandrino, M. Jenko, V. Martin, *Appl. Catal., A* **2001**, *206*, 113.

[10] J. Du, H. Li, C. Wang, A. Zhang, Y. Zhao, Y. Luo, *Catal. Commun.* **2020**, *141*, 106012.

[11] Y. Shao, Z. Xu, H. Wan, H. Chen, F. Liu, L. Li, S. Zheng, *J. Hazard. Mater.* **2010**, *179*, 135.

[12] H. Cai, Q. Zhang, X. Liu, Y. Li, M. Wang, G. Gao, Z. Meng, H. Sun, X. Hao, *Chem. Eng. J.* **2024**, *499*, 156261.

[13] Q. Zhang, H. Cai, X. Liu, Y. Li, M. Wang, G. Gao, Z. Meng, H. Sun, X. Hao, *Chem. Eng. J.* **2024**, *493*, 152570.

[14] C. Y. Zhang, C. Q. Zhang, G. W. Sun, J. L. Pan, L. Gong, G. Z. Sun, J. J. Biendicho, L. Balcells, X. L. Fan, J. R. Morante, J. Y. Zhou, A. Cabot, *Angew. Chem., Int. Ed.* **2022**, *61*, 202211570.

[15] Z. Du, Z. Meng, X. Gong, Z. Hao, X. Li, H. Sun, X. Hu, S. Yu, H. Tian, *Angew. Chem., Int. Ed.* **2024**, *63*, 2209794.

[16] H. Fang, S. Zhang, X. Wu, W. Liu, B. Wen, Z. Du, T. Jiang, *J. Power Sources* **2013**, *235*, 95.

[17] X. Xiao, T. Li, P. Yang, Y. Gao, H. Jin, W. Ni, W. Zhan, X. Zhang, Y. Cao, J. Zhong, L. Gong, W.-C. Yen, W. Mai, J. Chen, K. Huo, Y.-L. Chueh, Z. L. Wang, J. Zhou, *ACS Nano* **2012**, *6*, 9200.

[18] Z. Peng, R. Ye, J. A. Mann, D. Zakhidov, Y. Li, P. R. Smalley, J. Lin, J. M. Tour, *ACS Nano* **2015**, *9*, 5868.

[19] W. Shi, Z. Meng, Z. Xu, J. Xu, X. Sun, H. Nan, C. Zhang, S. Yu, X. Hu, H. Tian, *J. Mater. Chem. A* **2023**, *11*, 1369.

[20] M. F. El-Kady, V. Strong, S. Dubin, R. B. Kaner, *Science* **2012**, *335*, 1326.

[21] H. Nan, K. Song, J. Xu, S. Lv, S. Yu, X. Hu, H. Tian, *Acta Mater.* **2023**, *257*, 119174.

[22] J. Li, S. Luo, B. Zhang, J. Lu, W. Liu, Q. Zeng, J. Wan, X. Han, C. Hu, *Nano Energy* **2021**, *79*, 105410.

[23] J. Zhang, Z. Du, T. Yan, F. Zeng, Z. Xu, J. Xu, Z. Meng, X. Hu, J. Zhao, H. Tian, *Energy Storage Mater.* **2023**, *60*, 102831.

[24] Z. Meng, J. Xu, P. Yu, X. Hu, Y. Wu, Q. Zhang, Y. Li, L. Qiao, Y. Zeng, H. Tian, *Chem. Eng. J.* **2020**, *400*, 125966.

[25] C. Huang, Z. Jiang, F. Liu, W. Li, Q. Liang, Z. Zhao, X. Ge, K. Song, L. Zheng, X. Zhou, S. Qiao, W. Zhang, W. Zheng, *Angew. Chem., Int. Ed.* **2024**, *63*, 2405592.

[26] Z. Meng, H. Xu, Z. Du, Z. Xu, J. Xu, W. Zhang, X. Hu, H. Sun, H. Tian, J. Xu, W. Zheng, S. Dai, *Mater. Today* **2024**, *80*, 167.

[27] Z. Chen, W. Gong, J. Wang, S. Hou, G. Yang, C. Zhu, X. Fan, Y. Li, R. Gao, Y. Cui, *Nat. Commun.* **2023**, *14*, 5363.

[28] L. Rodriguez-Gonzalez, U. Simon, *Meas. Sci. Technol.* **2010**, *21*, 027003.

[29] Z. Du, Z. Meng, C. Jiang, C. Zhang, Y. Cui, Y. Li, C. Wang, X. Hu, S. Yu, H. Tian, *J. Energy Chem.* **2023**, *84*, 112.

[30] Z. Du, Z. Meng, H. Sun, Y. Li, C. Jiang, Y. Li, X. Hu, Y. Cui, S. Yu, H. Tian, *J. Energy Chem.* **2024**, *92*, 52.